Journal of Iraqi Al-Khwarizmi (JIKh) Volume:10 Issue:2 Year: 2026 pages: 658-676

Mathematical Modeling of Electro-Osmotic and Peristaltic Transport of Williamson Nanofluids in a Rotating Inclined Non-Uniform Biological Channels under Multi-Physical Fields

Authors Names

Hawraa Ahmed Abdul-Zahra[1], *Hayat Adel Ali*[2], *Shaymaa H. Salih*[3*]

Publication date: 14 /11 /2026

Keywords: Williamson fluid, Peristaltic flow, Inclined Magnetohydrodynamics (MHD), Electro-osmotic effect, Nanofluid.

ABSTRACT

This study investigates the combined electro-osmotic and peristaltic transport of a viscoelastic Williamson nanofluid through an inclined, non-uniformly tapered asymmetric channel embedded in a porous medium under multi-physical interactions. The mathematical formulation accounts for inclined magnetohydrodynamics (MHD), axis rotation, thermal radiation, cross-diffusion (Soret effect), velocity and thermal slip conditions, chemical reactions, and wall flexibility. The unsteady two-dimensional governing equations for mass, momentum, energy, and concentration conservation are formulated in a Cartesian coordinate system. Long-wavelength ($\delta \ll 1$) and low Reynolds number ($Re \to 0$) approximations based on lubrication theory are employed to simplify the governing equations, while the Debye–Hückel linearization approximation is utilized to resolve the electrohydrodynamic problem. Numerical solutions for axial velocity, temperature, concentration, and pressure rise are obtained using the NDSolve routine in Mathematica. The influence of the Helmholtz–Smoluchowski velocity, rotation parameter, electro-osmotic parameter, Joule heating, and Soret number is examined and graphically analyzed. Results indicate that the electric field and rotational motion enhance fluid velocity, whereas an increasing Hartmann number suppresses velocity due to resistive Lorentz forces. Additionally, temperature and concentration profiles increase with higher first-order chemical reaction parameters and Soret numbers.

Table 1(Nomenclature)

symbol	Definiton	Units/Type
d	The half-width of the channel at the inlet	m
$a_1,\ a_2$	Wave amplitudes	m
$\acute{\omega}$	is the non-uniformity tapering parameter	m
B_0	Uniform magnetic field strength	$T(Wb/m^2)$
c	Wave propagation speed	m/s
$\tilde{P}$	Fluid pressure	N/m^2
Q_0	Flow rate	
μ_f	Fluid viscosity	
K	Thermal conductivity	
K_r	First- order chemical reaction	
$\tilde{U}$,$\tilde{V}$	Velocity components in $\tilde{X}$ and $\tilde{Y}$ directions	m/s
C	Nanoparticle concentration	kg/m^3
C_0,C_1	Reference and wall concentration	kg/m^3
c_p	Specific heat capacity	$J/(kg.K)$
D_B	Brownian diffusion coefficient	m^2/s

[1]Department of Mathematics and Computer Applications, College of Applied sciences, University of Technology-Iraq, Baghdad, Iraq
[2]Department of Mathematics and Computer Applications, College of Applied sciences, University of Technology-Iraq, Baghdad, Iraq
[3]Department of Mathematics and Computer Applications, College of Applied sciences, University of Technology-Iraq, Baghdad, Iraq
[*]Corresponding: Hayat.A.Ali@uotechnology.edu.iq

g	Acceleration due to gravity	m/s^2
Ec	Eckert number	Dimensionless
M	Hartmann number (Magnetic parameter)	Dimensionless
N_b	Brownian motion parameter	Dimensionless
N_t	Thermophoresis parameter	Dimensionless
Pr	Prandtl number	Dimensionless
Re	Reynolds number	Dimensionless
T	Fluid temperature	K
T_0,T_1	Reference and wall temperatures	K
We	Williamson fluid parameter	Dimensionless
α	Thermal diffusivity	m^2/s
β_T,β_C	Thermal and concentration expansion coefficients	K^{-1},m^3/kg
Γ	Williamson time constant	s
λ	Peristaltic wavelength	m
μ_0	Zero-shear-rate dynamic viscosity	$kg/(m.s)$
ν	Kinematic viscosity	m^2/s
ρ	Fluid density	kg/m^3
σ^*	Electrical conductivity	S/m
θ	Dimensionless temperature	Dimensionless
σ	Dimensionless concentration	Dimensionless

1. Introduction

Peristaltic transport is a basic way our bodies move fluids, using waves that squeeze or relax a flexible tube or channel. This process is key to many important functions like pushing blood through tiny vessels, moving urine from the kidneys to the bladder, guiding food through our digestive system, and even helping sperm travel in the reproductive system. It's nature's way of gently but effectively pushing things along inside us. Recently bio-engineers have been using peristaltic pumping techniques to create new kinds of medical devices. Things like roller pumps, heart-lung machines, and tiny lab-on-a-chip systems have all been developed using this approach [1-4]. Latham [3] and Shapiro et al. [4] pioneered the theoretical understanding of this mechanism, which numerous subsequent studies have extended across various fluids and assumptions [5-8].

To accurately predict the flow behavior of biological and industrial fluids that deviate from classical Newtonian laws, various constitutive models have been established. Standard linear models fail to capture the shear-rate-dependent viscosity typical of physiological bio-fluids such as blood, chyme, and synovial fluid. Among these formulations, the Williamson fluid model originally introduced to describe non-Newtonian flow behavior has gained significant prominence due to its ability to incorporate both zero μ_0 and infinite μ_∞ shear-rate dynamic viscosities. This feature makes the Williamson model particularly effective for modeling shear-thinning phenomena in narrow biological ducts where local shear rates vary drastically. Consequently, theoretical and numerical investigations into peristaltic transport have increasingly relied on the Williamson constitutive equation across diverse

configurations. For instance, Nadeem et al. [9] investigated the combined effects of heat transfer and chemical reactions on the peristaltic motion of a Williamson fluid in an inclined asymmetric channel. Building on magnetic field interactions, Akram et al. [10] presented numerical and analytical treatments for Williamson fluid flow under induced magnetic fields. Hayat et al. [11] extended the analysis to include thermal and solutal transport by examining Soret and Dufour cross-diffusion effects in a convective-walled channel, while Reddappa et al. [12] examined the flow of a conducting Williamson fluid moving through a porous medium. Furthermore, Al-Khafajy and Al-Delfi [13] evaluated the influence of channel wall flexibility on flow behavior, and MM et al. [14] incorporated electro-osmotic mechanisms alongside activation energy in Williamson nanofluids. Together, these studies highlight the importance of accounting for non-Newtonian effects under complex physical conditions.

In recent years, integrating electro-osmotic mechanisms into bio-fluid transport has attracted significant research interest due to its ability to precisely regulate microfluidic devices and lab-on-a-chip technologies. Electro-osmosis arises when an external axial electric field interacts with mobile ions within the electric double layer (EDL) near charged channel walls, generating a bulk electrohydrodynamic force that acts alongside mechanical wall contractions. Under the Debye–Hückel linearization approximation, this secondary driving force alters the core hydrodynamic, thermal, and species transport behavior within complex micro-channels. Studies demonstrate that electro-kinetic parameters, such as the Helmholtz–Smoluchowski velocity (U_{hs}) and the electro-osmotic parameter (m_e), play a vital role in elevating axial velocity, modulating required pressure gradients, and controlling the size and trapping of fluid boluses. For instance, Bandopadhyay et al. (2016) demonstrated that electroosmosis-modulated peristaltic transport provides an effective, highly adaptable mechanism for flow control in microfluidic channels. Building upon these principles, MM et al. (2024) investigated the electro-osmotic peristaltic flow of a non-Newtonian Williamson nanofluid, showing that applying electro-kinetic forces substantially influences both velocity profiles and combined heat-mass transfer mechanisms in complex physiological and micro-scale environments.

Despite these valuable contributions, a significant research gap remains regarding the comprehensive interaction between electro-osmotic mechanisms, inclined magnetohydrodynamics (MHD), frame rotation, and cross-diffusion effects in non-Newtonian bio-fluids flowing through geometrically realistic biological ducts. Existing literature has largely evaluated electro-osmotic peristaltic flows in uniform, static, or fully symmetric geometries, neglecting the physical complexities posed by non-uniformly tapered asymmetric channels, porous media, and multi-physical force balances. To bridge this gap, the present study develops a detailed mathematical model to investigate the combined electro-osmotic and peristaltic transport of a non-Newtonian Williamson nanofluid moving through an inclined, non-uniformly tapered asymmetric channel embedded in a porous medium within a rotating frame. By incorporating boundary velocity/thermal slip, wall flexibility, thermal radiation, chemical reactions, and the Soret effect, this work provides a complete framework for analyzing flow dynamics, thermal dissipation, mass transfer, and trapping phenomena in complex biomedical systems.

The remainder of this paper is organized as follows: Section 2 formulates the mathematical model, detailing the governing physical equations, boundary conditions, and the application of the Debye–Hückel linearization along with the long-wavelength ($\delta \ll 1$) and low Reynolds number ($Re \to 0$)approximations. Section 3 outlines the numerical scheme implemented using the NDSolve procedure in Mathematica. Section 4 provides a comprehensive graphical discussion analyzing the physical effects of key parameters on the velocity, temperature, concentration, pressure gradient, pumping, and

streamline trapping mechanism. Finally, Section 5 summarizes the main findings and highlights the biological significance of the study.

2. Methodology and Problem Formulation

We examine the peristaltic flow of a two dimensional, incompressible, electrically conducting Williamson nanofluid flowing through a porous medium in a non-uniform asymmetric channel having a width $(2d)$, is inclined at an angle ϑ relative to the horizontal axis and rotates uniformly around the horizontal with un angular velocity $\widetilde{\Omega}$ (see Fig. 1). The fluid domain is geometrically bounded by upper and lower flexible walls governed by sinusoidal wave profiles. An inclined magnetic field of strength $B_0 = (\beta_0 \sin\beta, \beta_0 \cos\beta)$ is applied at an angle β, the induced magnetic field is neglected due to the low magnetic Reynolds number approximation. A peristaltic wave train is progressing down the length of an asymmetric channel wall with a constant wave speed c and wavelength λ. The time-dependent deformation of the upper and lower boundaries is mathematically expressed respectively as:

$$\tilde{Y}_1=\widetilde{H}_1(\tilde{X},\tilde{t}) = d + \acute{\omega}\,\tilde{X} + a_1 sin\left(\frac{\pi}{\lambda}(\tilde{X}-c\tilde{t})\right) cos\left(\frac{\pi}{\lambda}(\tilde{X}-c\tilde{t})\right), \quad (1)$$

$$\tilde{Y}_2=\widetilde{H}_2(\tilde{X},\tilde{t}) = -d - \acute{\omega}\,\tilde{X} - a_2 sin\left(\frac{\pi}{\lambda}(\tilde{X}-c\tilde{t})+\phi\right) cos\left(\frac{\pi}{\lambda}(\tilde{X}-c\tilde{t})+\phi\right). \quad (2)$$

ϕ is the phase difference ranging between $(0 \le \phi \le \pi)$, in which $(\phi = 0)$ corresponds to symmetric in-phase wave propagation, whereas $(\phi = \pi)$ refers to out of phase motion. To prevent wall intersection, the channel parameters satisfy the geometric constraint $a_1^2 + a_2^2 + 2\,a_1\,a_2\,\cos\phi \le (2d)^2$.

The mathematical formula of basic governing equations is.

$$\frac{\partial\widetilde{U}}{\partial\tilde{X}} + \frac{\partial\widetilde{V}}{\partial\tilde{Y}} = 0, \quad (3)$$

$$\rho_f\left(\frac{\partial\widetilde{U}}{\partial\tilde{t}} + \widetilde{U}\frac{\partial\widetilde{U}}{\partial\tilde{X}} + \tilde{V}\frac{\partial\widetilde{U}}{\partial\tilde{Y}}\right) - \rho_f\,\widetilde{\Omega}\left(\widetilde{\Omega}\,\widetilde{U}+2\frac{\partial\widetilde{V}}{\partial\tilde{t}}\right) = \frac{-\partial\tilde{P}}{\partial\tilde{X}} + \frac{\partial\tilde{S}_{\tilde{X}\tilde{X}}}{\partial\tilde{X}} + \frac{\partial\tilde{S}_{\tilde{X}\tilde{Y}}}{\partial\tilde{Y}} - \sigma^*{\beta_0}^2\,cos\beta\left(\widetilde{U}\,cos\beta - \tilde{V}\,sin\beta\right) - \frac{\mu_f}{\kappa_0}\widetilde{U} + P_e\,E_x + \rho_f g\ sin\vartheta\ , \quad (4)$$

$$\rho_f\left(\frac{\partial\widetilde{V}}{\partial\tilde{t}} + \widetilde{U}\frac{\partial\widetilde{V}}{\partial\tilde{X}} + \tilde{V}\frac{\partial\widetilde{V}}{\partial\tilde{Y}}\right) - \rho_f\,\widetilde{\Omega}\left(\widetilde{\Omega}\,\tilde{V}-2\frac{\partial\widetilde{U}}{\partial\tilde{t}}\right) = \frac{-\partial\tilde{P}}{\partial\tilde{Y}} + \frac{\partial\tilde{S}_{\tilde{Y}\tilde{X}}}{\partial\tilde{X}} + \frac{\partial\tilde{S}_{\tilde{Y}\tilde{Y}}}{\partial\tilde{Y}} - \sigma^*{\beta_0}^2\,sin\beta\left(\widetilde{U}\,cos\beta - \tilde{V}\,sin\beta\right) - \frac{\mu_f}{\kappa_0}\widetilde{U}\ , \quad (5)$$

$$\rho C_p\left(\frac{\partial T}{\partial\tilde{t}} + \widetilde{U}\frac{\partial T}{\partial\tilde{X}} + \tilde{V}\frac{\partial T}{\partial\tilde{Y}}\right) = K\left(\frac{\partial^2 T}{\partial\tilde{X}^2} + \frac{\partial^2 T}{\partial\tilde{Y}^2}\right) - Q_0(T-T_0) + \frac{\partial\widetilde{U}}{\partial\tilde{X}}\tilde{S}_{\tilde{X}\tilde{X}} + \frac{\partial\widetilde{U}}{\partial\tilde{Y}}\tilde{S}_{\tilde{X}\tilde{Y}} + \frac{\partial\widetilde{V}}{\partial\tilde{X}}\tilde{S}_{\tilde{Y}\tilde{X}} + \frac{\partial\widetilde{V}}{\partial\tilde{Y}}\tilde{S}_{\tilde{Y}\tilde{Y}} + \sigma^*{\beta_0}^2\,cos\beta\,\widetilde{U}^2 - \frac{\partial q_r}{\partial\tilde{Y}} + P_e\,{E_x}^2, \quad (6)$$

$$\left(\frac{\partial C}{\partial\tilde{t}} + \widetilde{U}\frac{\partial C}{\partial\tilde{X}} + \tilde{V}\frac{\partial C}{\partial\tilde{Y}}\right) = D_B\left(\frac{\partial^2 C}{\partial\tilde{X}^2} + \frac{\partial^2 C}{\partial\tilde{Y}^2}\right) - K_r(C-C_0) + \frac{D_B\,K_T}{T_m}\left(\frac{\partial^2 T}{\partial\tilde{X}^2} + \frac{\partial^2 T}{\partial\tilde{Y}^2}\right). \quad (7)$$

Where $\vec{V} = \left(\widetilde{U}(\tilde{X},\tilde{Y},\tilde{t}), \tilde{V}(\tilde{X},\tilde{Y},\tilde{t})\right)$ is the velocity field.

The radiative heat flux in the $\tilde{X}$-direction is assumed by adopting Rosseland approximation as [32]:

$$q_r = \frac{4\,\sigma_s^*}{3K^*}\frac{\partial T^4}{\partial\tilde{Y}}\,, \quad (8)$$

σ_s^* and K^* are the Stefan-Boltzmann constant and the mean absorption coefficient, respectively.

By assuming a sufficiently small temperature variation across the flow, the term T^4 can be approximated using a Taylor series expansion around T_1, yielding:

$$T^4 \cong {T_1}^4 + 4{T_1}^3(T-T_1) + 6{T_1}^2(T-T_1)^2 + , \quad (9)$$

Neglecting the higher-order terms beyond the first-order derivative in Equation (9), and substituting the reduced terms into Equation (13) simplifies the expression to:

$$q_r = \frac{16{T_1}^3 \sigma_s^*}{3K^*}. \quad (10)$$

$\bar{S}$ is the Cauchy stress tensor for the Willamson fluid model that expressed as follows:

$$\bar{S} = [\mu_\infty + (\mu_0 - \mu_\infty)/(1 - \Gamma\dot{\gamma})]\dot{\gamma} \quad (11)$$

Where Γ is the Willamson parameter, $\dot{\gamma} = \sqrt{\frac{1}{2}\pi}$ and $\Pi = \left(trace\left(grad\,\tilde{V} + \left(grad\,\tilde{V}\right)^T\right)\right)^2$ is the rate of strain, μ_∞ and μ_0 are zero and infinite shear viscosities. For Simplification suppose $(\mu_\infty \to 0)$ we get.

$$\bar{S} = \mu_0\dot{\gamma}/(1 - \Gamma\dot{\gamma}) \cong \mu_0(1 - \Gamma\dot{\gamma})\dot{\gamma} \quad (12)$$

The problem is subjected to the following boundary conditions:

- Velocity slip conditions.

$$\widetilde{U} = -L\frac{\partial\widetilde{U}}{\partial\tilde{Y}}, \quad \psi = \frac{F}{2}, \; at \quad \tilde{Y}_1 = \widetilde{H}_1, \quad (13)$$

$$\widetilde{U} = L\frac{\partial\widetilde{U}}{\partial\tilde{Y}}, \quad at \quad \tilde{Y}_2 = \widetilde{H}_2 \quad (14)$$

- Thermal boundary conditions.

$$-K_f\frac{\partial T}{\partial\tilde{Y}} = h_s(T_0 - T), \quad at \; \tilde{Y}_1 = \widetilde{H}_1 \quad (15)$$

$$K_f\frac{\partial T}{\partial\tilde{Y}} = h_s(T - T_1), \quad at \quad \tilde{Y}_2 = \widetilde{H}_2 \quad (16)$$

- Concentration boundary conditions

$$-K_m\frac{\partial C}{\partial\tilde{Y}} = -h_m(C_0 - C), \quad at \; \tilde{Y}_1 = \widetilde{H}_1 \quad (17)$$

$$-K_n\frac{\partial C}{\partial\tilde{Y}} = -h_m(C - C_1), \quad at \quad \tilde{Y}_2 = \widetilde{H}_2$$

The Wall Properties is:

$$L\left(\widetilde{H}\right) = \left(m_0\frac{\partial^2\widetilde{H}}{\partial\tilde{t}^2} + d_0\frac{\partial\widetilde{H}}{\partial\tilde{t}} + B_{ei}\frac{\partial^4\widetilde{H}}{\partial\tilde{X}^4} - T_s\frac{\partial^2\widetilde{H}}{\partial\tilde{X}^2} + G\widetilde{H}\right) = \bar{P} - P_0 \quad (18)$$

To govern the electro-osmotic transport within the electric double layer, the Poisson–Boltzmann equation is used to model the relationship between spatial charge density P_e and electrical potential $\bar{\varphi}$ as:

$$\nabla^2\bar{\varphi} = \frac{-P_e}{\epsilon_0} \quad (19)$$

$$\frac{\partial^2\bar{\varphi}}{\partial\tilde{Y}^2} = \frac{-P_e}{\epsilon_0} \quad (20)$$

Where P_e is given as []:

$$P_e = -ez(\bar{n}_+ - \bar{n}_-) \quad (21)$$

$$\bar{n}_\pm = n_0 e\left(\pm\frac{ez\bar{\varphi}}{K_B Tav}\right) \quad (22)$$

where $e, z, \bar{n}_+, \bar{n}_-, Tav, K_B$ and n_0 are represent the electric charge, charge balance, the number of densities of positive (cations) and negative (anions), average temperature, Boltzmann constant and bulk ions concentration respectively.

Furthermore, the implementations of Debye-Huckle linearization and lubrication approach transforms equation (20)

$$\frac{\partial^2\varphi}{\partial y^2} = {m_e}^2\varphi \tag{23}$$

Where $m_e = dez\sqrt{\frac{2n_0}{\epsilon_0 K_B T ar}} = \frac{a}{\lambda_D}$ is the electroosmotic parameter and λ_D is the Debye length/thickness of electrical double layer.

equation (23) is subjected to the following boundary conditions:

$$\varphi = 1 \; at \; y = h_1, \quad \frac{\partial\varphi}{\partial y} = 0, at \quad y = h_2 \tag{24}$$

Solving equation (23) and (24) we get.

$$\varphi = \frac{sinh\, m_e(y-h_1)}{sinh\, m_e(h_1-h_2)} \tag{25}$$

Identifying a wave frame $(\bar{x}, \bar{y})$ and the relationship with the fixed frame $(\check{X}, \check{Y}, \tilde{t})$ by the expression.

$$\bar{x} = \tilde{X} - c\tilde{t}, \bar{y} = \tilde{Y}, \bar{u} = \tilde{U} - c, \; \bar{v} = \tilde{V}, \; \bar{p}(\bar{x}) = \tilde{P}(\tilde{X}, \tilde{t}, \tag{26}$$

Using the following dimensionless magnitudes:

$$\left.\begin{aligned} x = \frac{\bar{x}}{\lambda}, y = \frac{\bar{y}}{d}, u = \frac{\bar{u}}{c}, v = \frac{\bar{v}}{c\delta}, h_1 = \frac{\bar{H}_1(\check{X})}{d}, h_2 = \frac{\bar{H}_2(\check{X})}{d}, \delta = \frac{d}{\lambda}, We = \frac{\Gamma c}{d}, Ha = \sqrt{\frac{\sigma_{nf}{B_0}^2 d^2}{\mu_f}}, \\ , p = \frac{d^2\bar{p}(X)}{\lambda\mu_f c}, \; S_r = \frac{\rho D_B K_T (T_1-T_0)}{\mu_f T_m (C_1-C_0)}, Pr = \frac{D_B c\rho}{K_f}, D1 = \frac{Q_0}{K(T_1-T_0)}, D2 = \frac{k_r}{D(C_1-C_0)} \\ , Rn = \frac{16\,{T_1}^3\sigma^*}{3\,k^*\mu_f}, Da = \frac{\kappa_0}{d^2}, \epsilon_1 = \frac{b_1}{d}, Br = P_r Ec \\ \epsilon_2 = \frac{b_2}{d}, \acute{\psi}(\bar{x}, \bar{y}) = \frac{\psi}{cd} \;\; \varpi = \frac{\acute{\varpi}\lambda}{d}, Re = \frac{\rho c d}{\mu}, \theta = \frac{T-T_0}{T_1-T_0}, \sigma = \frac{C-C_0}{C_1-C_0}, \gamma = \frac{\rho_f d^2\Omega^2}{\mu_f} \\ , Ec = \frac{c^2}{C_p(T_1-T_0)}, S_c = \frac{\mu_f}{\rho D_B}, E1 = \frac{d^3 B_{ei}}{\lambda^5\mu_f c}, E2 = \frac{T_s d^3}{\lambda^3\mu_f c}, E3 = \frac{d^3 G}{\mu_f c\lambda} \\ \alpha_1 = \frac{\beta_1}{d}, \alpha_2 = \frac{\beta_2}{d}, D4 = \frac{\sigma d^2 {E_x}^2}{K(T_1-T_0)}, Uhs = \frac{Pe\epsilon_0 E_x}{\mu_f c\lambda}. \end{aligned}\right\} \tag{27}$$

In which $\varpi, Ha, Re, \delta, Da, Pr, E_c, S_r, Rn, S_c, D4, Uhs$ are the non-uniform parameter, Hartmann number, Reynolds number, the dimensionless number of waves, permeability parameter, Prandtl number, Eckert number, Soret number, dimensionless thermal radiation, Schmidt number, joule heating, Helmholtz-Smoluchowski velocity. Additionally, the velocity components are related to the stream function $\psi(x, y)$ via the following expressions:

$$u = \frac{\partial\psi}{\partial y}, \; v = -\delta\frac{\partial\psi}{\partial x}. \tag{28}$$

Substituting equations (26) and (27) into equations (3)-(7) and (12)-(18), and by invoking the long-wavelength $(\delta \ll 1)$ and low-Reynolds-number $(Re \to 0)$ approximations, the continuity equation is identically satisfied, thereby reducing the remaining governing flow equations into the following dimensionless system:

$$\frac{\partial P}{\partial x} = \frac{\partial S_{xy}}{\partial y} + \gamma(u+1) - (Ha^2 cos\beta^2)(u+1) - \frac{1}{Da}(u+1) + {m_e}^2 U_{hs}\varphi + \frac{R_e}{F_r} sin\,\vartheta, \tag{29}$$

$$\frac{\partial p}{\partial y} = 0, \tag{30}$$

From Equation (30), it follows that the pressure is independent of y, where $\frac{\partial p}{\partial y} = 0$.

$$(1+R_n)\frac{\partial^2\theta}{\partial y^2}+ +D1\,\theta+Br\left(\frac{\partial u}{\partial y}S_{xy}\right)+Br\,Ha^2cos^2\beta(u+1)^2+D4=0, \quad (31)$$

$$\frac{\partial^2\sigma}{\partial y^2}+D2\,\sigma+S_cS_r\frac{\partial^2\theta}{\partial y^2}=0 \quad (32)$$

$$S_{xy}=-\left(1+We\frac{\partial u}{\partial y}\right)\left(\frac{\partial u}{\partial y}\right) \quad (33)$$

The dimensionless boundary conditions are:

$$\left.\begin{aligned} u=-1-\beta_1\frac{\partial u}{\partial y},\psi=-\frac{F}{2} \qquad at\ \ y=h_1=1+m_1(x+ct)+\epsilon_1 sin\left(\frac{\pi}{\lambda}x\right)cos\left(\frac{\pi}{\lambda}x\right)\\ u=-1+\beta_1\frac{\partial u}{\partial y},\ \psi=\frac{F}{2} \qquad at\ \ y=h_2=-1-m_1(x+ct)-\epsilon_2 sin\left(\frac{\pi}{\lambda}x+\emptyset\right)cos\left(\frac{\pi}{\lambda}x+\emptyset\right)\end{aligned}\right\} \quad (34)$$

The dimensionless thermal and concentration boundary conditions are:

$$\begin{aligned}&\theta+L1\frac{\partial\theta}{\partial y}=0 \quad ,\sigma+L2\frac{\partial\sigma}{\partial y}=0 \quad at\ y=h_1\\ &\theta-L1\frac{\partial\theta}{\partial y}=1 \quad ,\sigma-L2\frac{\partial\sigma}{\partial y}=1 \quad at\ y=h_2\end{aligned} \quad (35)$$

and the wall properties dimensionless equation is

$$E1\frac{\partial^4h(x)}{\partial x^4}-E2\frac{\partial^3h(x)}{\partial x^3}+E3\frac{\partial h(x)}{\partial x}=\frac{\partial P}{\partial x} \quad (36)$$

Substituting equation (36) into equation (29), we have.

$$E1\frac{\partial^4h(x)}{\partial x^4}-E2\frac{\partial^3h(x)}{\partial x^3}+E3\frac{\partial h(x)}{\partial x}=\frac{\partial S_{xy}}{\partial y}+\gamma(u+1)-(Ha^2cos\beta^2)(u+1)-\frac{1}{Da}(u+1)+ m_e{}^2U_{hs}\varphi+\frac{R_e}{F_r}sin\vartheta, \quad (37)$$

The dimensionless expression of pressure rise per wavelength is given as:

$$\Delta p_\lambda=\int_0^1\frac{\partial p}{\partial x}dx. \quad (38)$$

3. Numerical Solution

This section reviews the numerical results of velocity, temperature and stream function graphically. A numerical technique is employed to solve the system of nonlinear equations (28) -(33) with boundary conditions (31) -(37) since the exact solution is difficult to obtain. The solution is built on (ND Solve) command with Mathematica programing.

4. Graphical Discussions

This section presents a comprehensive graphical analysis aimed at exploring the physical influences of various emerging parameters on the velocity field, temperature distribution, pressure gradient, pressure rise, concentration profile, and the streamline trapping mechanism.

4.1. Velocity profile

The physical significance of these results is discussed here: Figures 2 & 3 represent the combined impact of Hartmann number Ha, permeability parameter Da, Weissenberg numbers we, rotation parameter γ , Helmholtz-Smoluchowski velocityU_{hs}, wall elasticity parameter $E1$ for fixed values of the variables $\{\phi = \frac{Pi}{6}, m_e = 0.3, \vartheta = \frac{Pi}{6}, \varpi = 0.5, \epsilon_1 = 0.01,\ \epsilon_2 = 0.03, Fr = 5, x = 0.5, Re = 0.2\ , \beta = \frac{Pi}{6}\ , U_{hs} = 0.3\ , \beta_1 = 0.5\ \}$upon the dimensionless axial velocity profile $u(y)$. Figure 2(a) demonstrates that the velocity profile shows suppressing effect for larger Hartman number Ha. This behavior physically holds because higher values of Hartmann number increase the Lorentz force which opposes the main flow causing its suppression. Figure 2(b) reveals that an increment in Da causes considerable amplification of the velocity profile. It may be due to higher permeability of the porous matrix decreasing the hydro- dynamic resistance and dragging forces experienced by the fluid as a result the velocity profile increases.

Figure 3(a) shows the impact on the axial velocity with an increasing value of We (Williamson parameter). According to the Williamson model, this means that our flow experiences the characteristic shear thinning properties. Therefore, the decrease in effective viscosity due to high local shear stress reduces viscous effects within the system, leading to increased movement around the core. Meanwhile, as seen from Figure 3(b), increasing the magnitude of elastic wall parameters E1 (wall tensions/stiffnesses) results in a reduction of the maximum value attained by axial velocity. This makes intuitive sense given the relationship between stiffness and damping systems where higher spring constants result in stronger restoring forces working against motion. In terms of physiological applications, this suggests that stiffer channels would reduce pumping efficiencies through peristalsis action. Figure 4(a) illustrates the effect of the Helmholtz–Smoluchowski velocity U_{hs}which is directly proportional to E_x on the fluid velocity profile. The plot shows that as U_{hs} increases i.e. $(E_x > 0)$, the velocity curves shift upward along the vertical axis. This occurs when the external electric field strength increases, the magnitude of the negative velocity decreases, demonstrating that the field effectively enhances the net flow across the channel. Figure 4(b) depicts that a larger wall elasticity $E1$parameter, diminishes the velocity profile across the channel.

(a) (b)

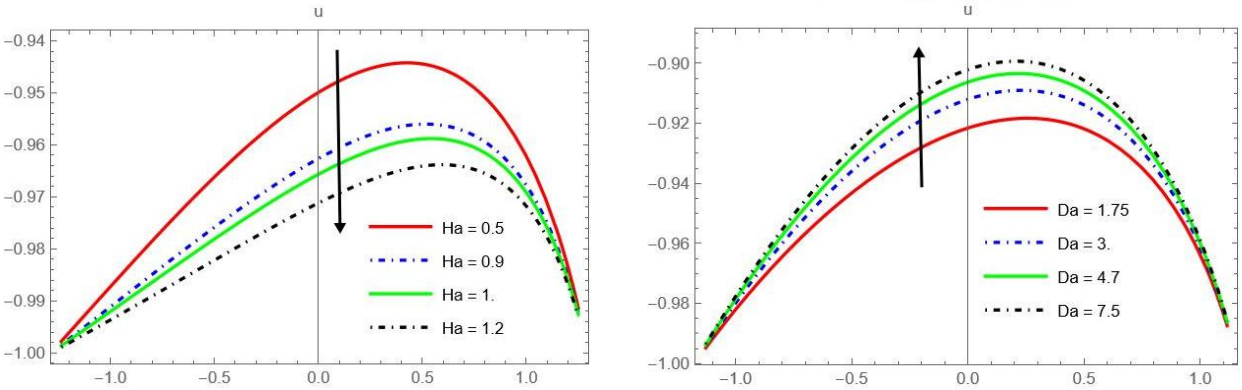


Figure 2: Velocity profile for different values of (a) Hartmann Number Ha (b) Darcy Number Da .

(a) (b)

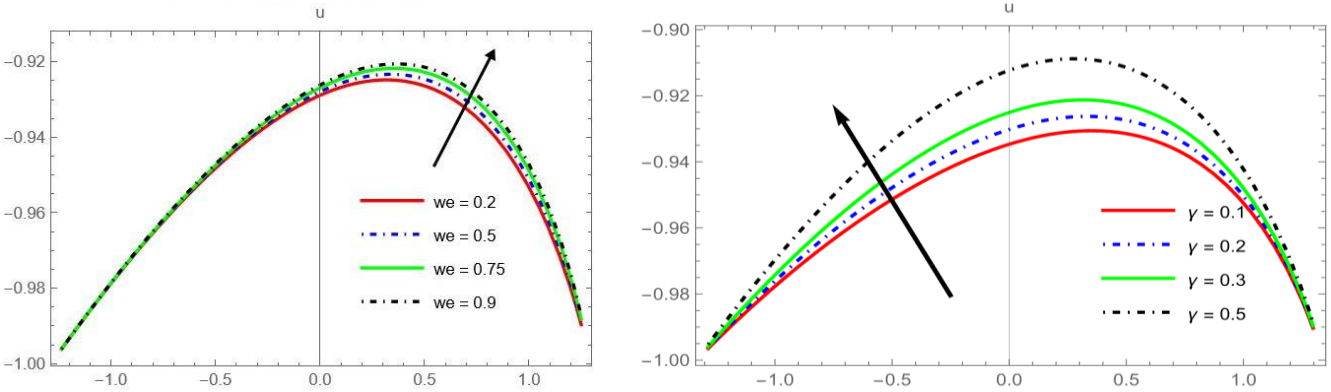


Figure 3: Velocity profile for different values of (a) Williamson Parameter We (b) Rotation parameter γ .

(a) (b)

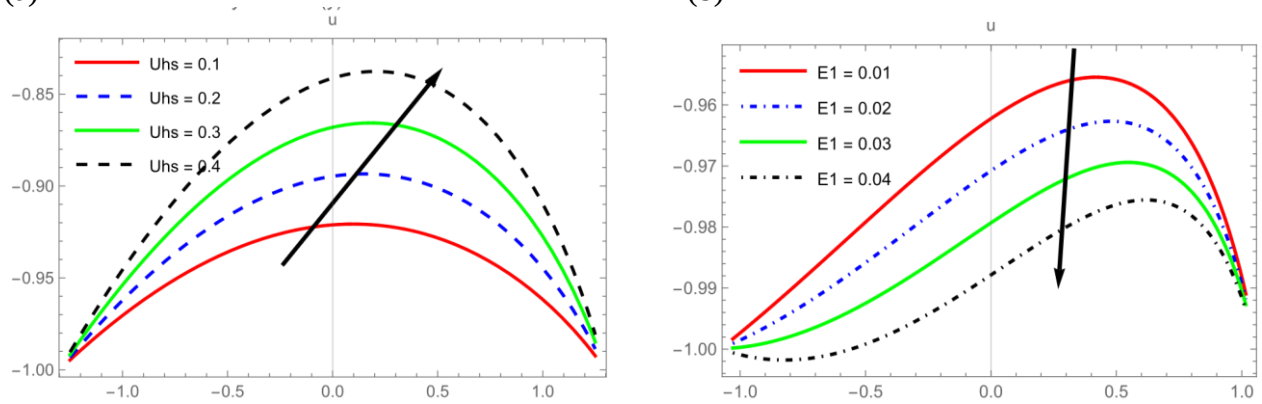


Figure 4: Velocity profile for different values of (a) Helmholtz–Smoluchowski velocity U_{hs} (b) Wall elasticity parameter $E1$.

4.2. Temperature Distribution

Figures 5-7 illustrate how the most emerging parameters: Brinkman Number Br , thermal radiation Rd, Hartmann number Ha, rotational Parameter γ, chemical reaction parameter $D1$, Williamson parameter We, influence the system's temperature distribution for fixed values of the variables $\{\phi = \frac{Pi}{6}, m_e = 0.3, \vartheta = \frac{Pi}{6}, \varpi = 0.5, \epsilon_1 = 0.01, \epsilon_2 = 0.03, Fr = 5, x = 0.5, Re = 0.2, \beta = \frac{Pi}{6}, U_{hs} = 0.3, \beta_1 = 0.5\}$. Figure 5(a) reveals that as Br increases, the temperature profile θ(y) rises across the channel. Physically this parameter measures the heat generated by viscous dissipation relative to conduction. Higher values of Br mean stronger internal fluid friction, which converts kinetic energy into thermal energy and heats the fluid up. Figure 5(b) shows that ascending thermal radiation parameter Rd values decrease the temperature profile. As (Rd) increases, enhances heat dissipation from the fluid layer to the environment, as a result the fluid temperature reduces. The graphical behavior of Ha parameter has been depicted through Figure 6(a). Increasing values of Ha cause θ(y) curve upward. Applying a magnetic field to an electrically conducting fluid enhances joule heating and resistive Lorentz forces, converting kinetic energy into the thermal energy [6]. This additional heat generation elevates fluid temperatures at high Ha. Figure 6(b) shows that increasing the rotation speed (via the rotation parameter γ) decreases the temperature profile particularly near the channel centerline. Since rotation introduces Coriolis forces that secondary-flow circulation patterns create, driving heat away from the central region toward the walls. This enhanced fluid mixing disrupts the core thermal buildup, resulting in a lower temperature along the centerline. Figure 7(a) records the direct effect of the chemical reaction parameter ($D1$) on the temperature profile. Physically, this represents an exothermic chemical reaction where higher reaction rates generate additional internal heat, in which increasing θ(y) profile. Higher values of *we* rise the fluid's temperature profile through channel see Figure 7(b). This impact due to enhance fluid's non-Newtonian shear-thinning behavior which leads to extra friction that raising the fluid temperature.

(a) (b)

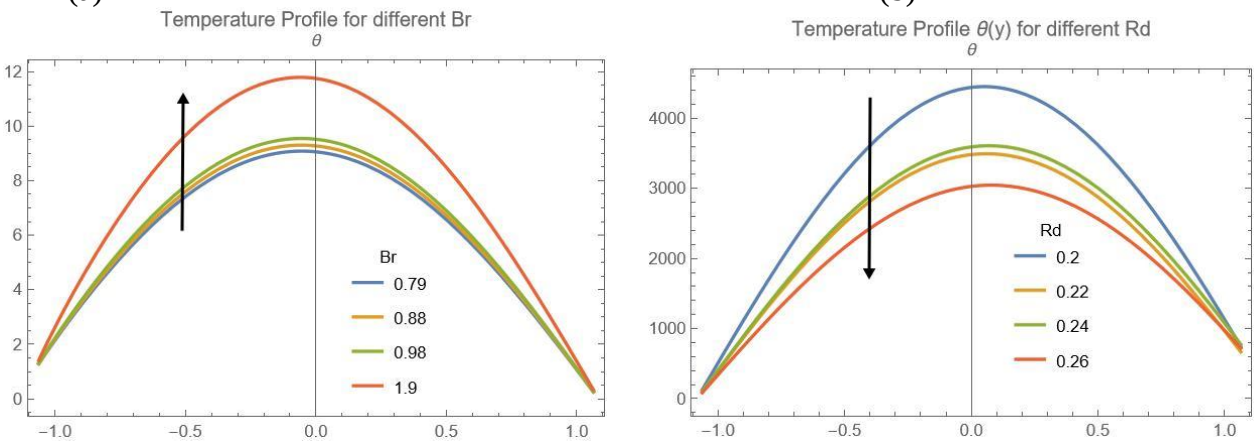


Figure 5: Temperature profile $\theta(y)$ for different values of (a) Brinkman Number Br (b) Radiation Parameter Rd.

(a) (b)

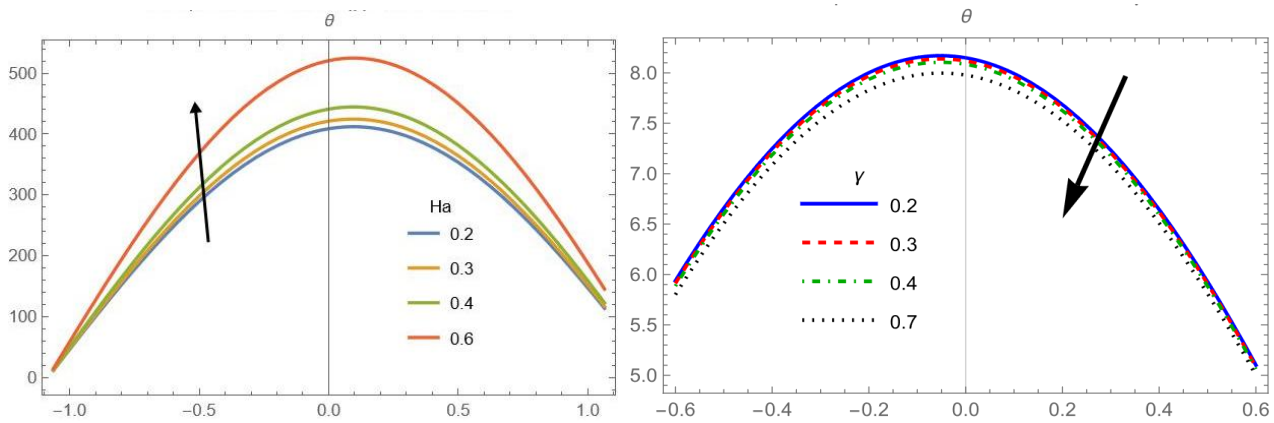


Figure 6: Temperature profile $\theta(y)$for different values of (a) Hartmann Number Ha (b) Rotation parameter γ.

(a) (b)

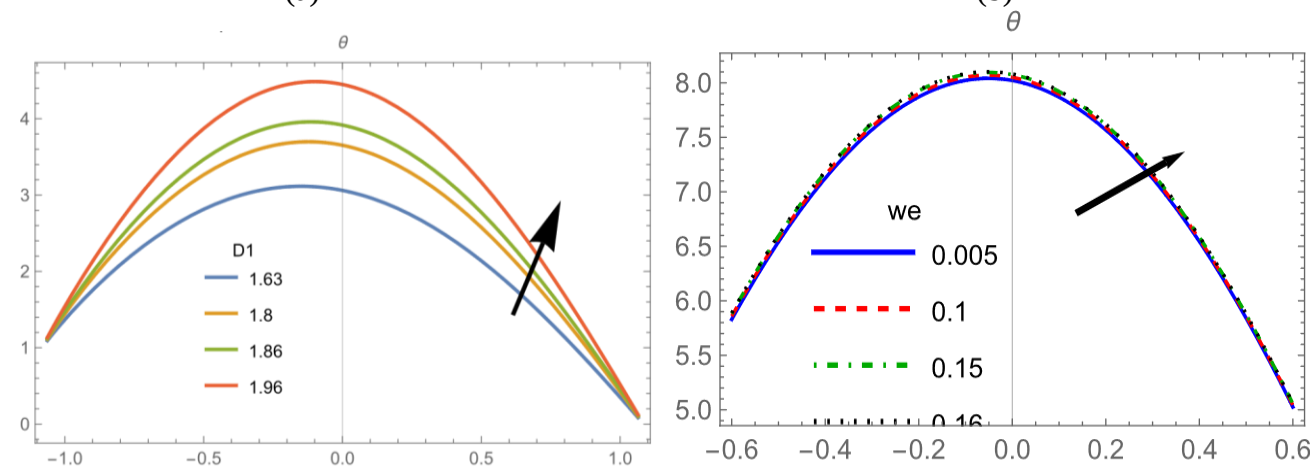


Figure 7: Temperature profile $\theta(y)$for different values of (a) chemical reaction parameter $D1$ (b) Willamson parameter we.

4.3. Pressure Gradient Profile

The variation of gradient pressure profile for important chosen parameters is analyzed through Figures 8 and 9. Figure 8(a) indicate that increasing the rotation parameter (γ) from 0.2 to 0.8 reduces the dp/dx curve over the length of channel. This drop occurs due to Coriolis force from rotation redistributes kinetic energy into lateral flows. This reduces resistance along the main flow direction, so a smaller dp/dx is required to drive the fluid. Figure 8(b) depicts an increment in dp/dx profile as electro-osmotic velocity U_{hs} rises. Physically, electro-osmotic acts as a secondary driving mechanism through peristalsis within the electric double layer EDL, which elevates the pressure gradients dp/dx to resist boundary friction and sustain the flow rate. From Figure 9(a), we observed that increasing the value of the Williamson parameter We, the magnitude of the dimensionless pressure gradient dp/dx decreases. This result occurs because the fluid exhibits shear-thinning nature, so stronger non-Newtonian effects lower its viscosity. Consequently, a smaller amount of pressure required to achieve the flow. From Figure 9(b), one can observe that increasing the electro-osmotic parameter m_e, elevates

the pressure gradient profiles. Higher values of m_e impart more kinetic energy to the charged fluid particles, enhancing fluid motion and thus requiring a higher-pressure gradient.

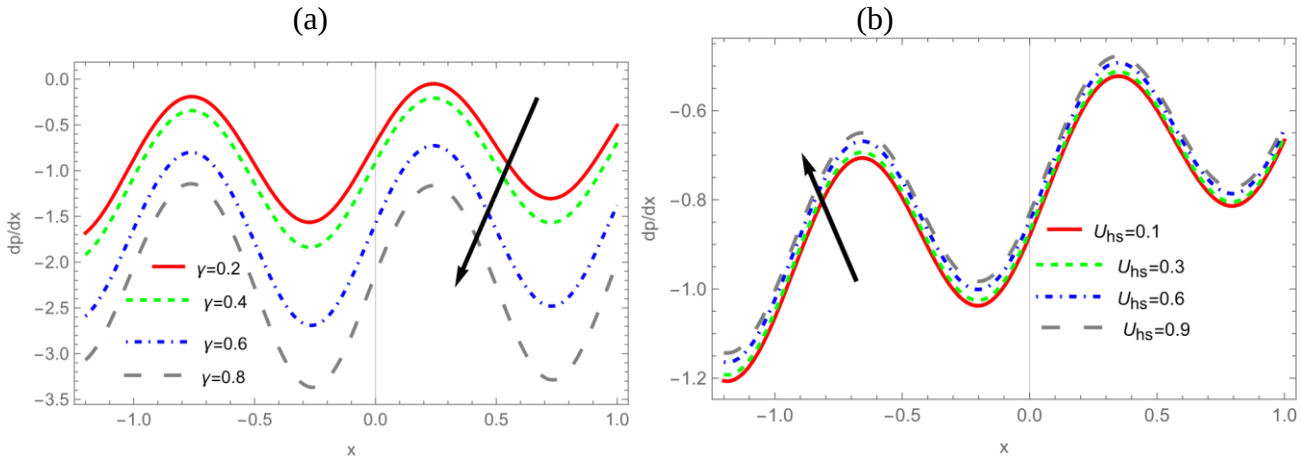


Figure 8: Gradient of pressure for variation of (a) Rotation Parameter γ (b) Helmholtz–Smoluchowski velocityU_{hs}.

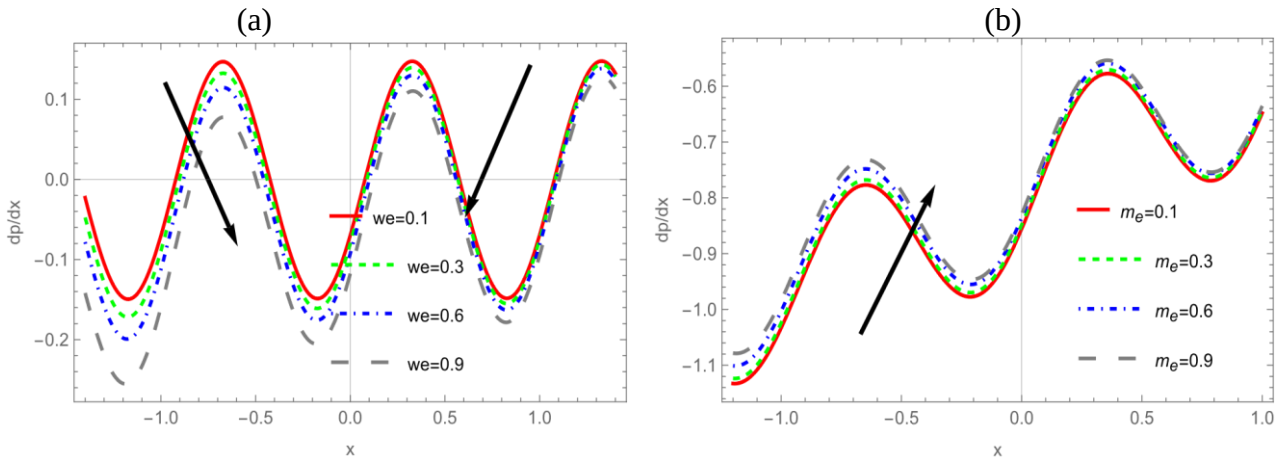


Figure 9: Gradient of pressure for variation of (a) Williamson Parameter We (b) Electro-osmotic parameter m_e.

4.4. Pressure Rise Pumping

Pressure rise (ΔP) is a physical measure of the total pressure difference generated across a single wavelength by the channel walls to overcome internal hydraulic, viscous, or magnetic resistance, ensuring the continuous forward transport of the fluid. The pressure rise per wavelength Δp_λ is divided into three flow regimes. The pumping regime $(\Delta p_\lambda > 0, \Theta > 0)$ is achieved when peristaltic wall motion contractions force the fluid forward. Fluid movement driven solely by peristaltic action is called a free pumping region $(\Delta p_\lambda = 0)$. In contrast, the co-pumping regime $(\Delta p_\lambda < 0, \Theta > 0)$ occurs when a favorable pressure gradient assists fluid flow. The discussion is evaluated for fixed parameters $(\alpha_1 = 0.1, \beta_1 = 0.3, m_e = 0.4, \phi = \frac{\mathrm{Pi}}{6}, y = 0.1, \varpi = 0.2, \mathrm{Re} = 0.2, \mathrm{Fr} = 0.2, \epsilon_1 = 0.01, \epsilon_2 =$

$0.02, c = 0.1, t = 0.1, \vartheta = \frac{\mathrm{Pi}}{6}$). Figure 10(a) plots the pressure rise (Δp_λ) for Hartmann number (H). As the value of Ha increases, Δp_λ increases in the peristaltic pumping region ($\Delta \mathrm{P} > 0, \Theta > 0$) and decreases in the co-pumping region, whereas free pumping occurs at ($\Theta = 2.2$). Conversely, Figures 10(b) and 11(a) record a drop in the peristaltic pumping region with higher Darcy number and rotation parameter γ respectively, compared to the retrograde region, which shows an increase. Furthermore, free pumping occurs at ($\Theta = 2.2$). The impact of Weissenberg number (We)on pumping is illustrated in Figure 11(b), where higher values of (We) decrease the pumping rate along the channel. This result is due to the diminishing effects of strong viscoelasticity that reduce internal fluid resistance, making the pumping mechanism less effective on the flow.

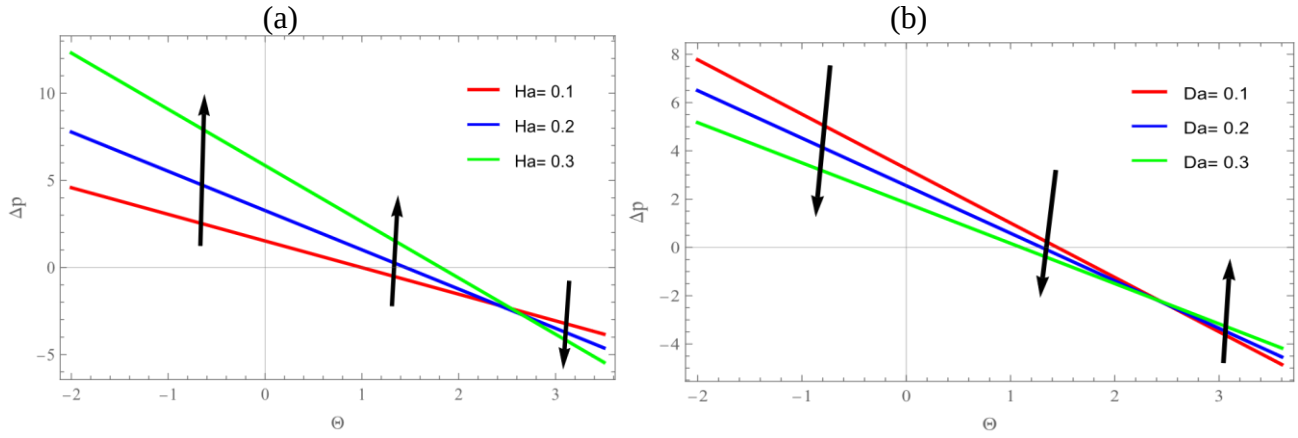


Figure 10: pressure rise for variation of (a) Hartmann number Ha (b) Darcy number Da.

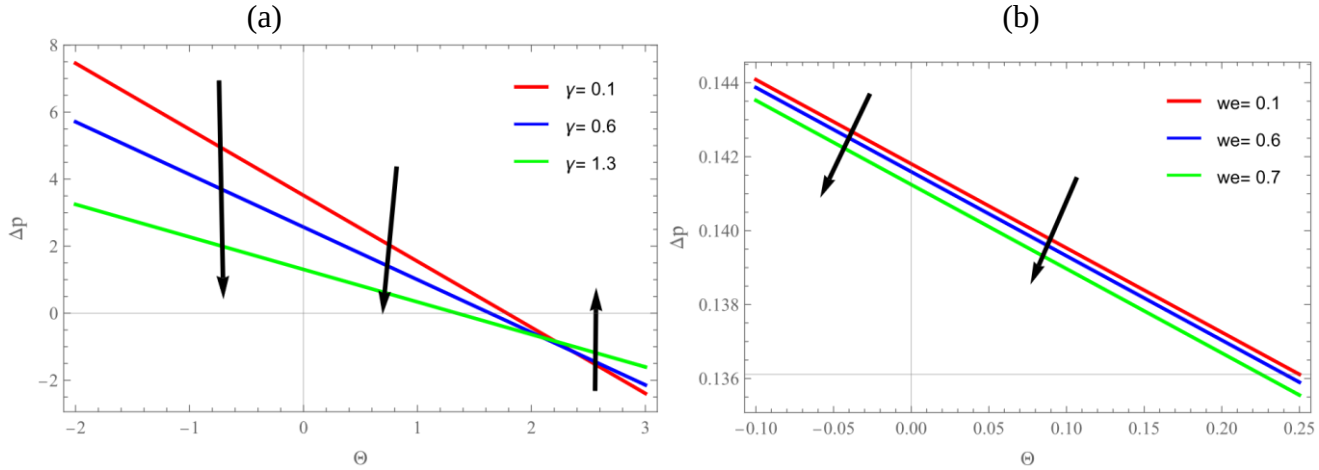


Figure 11: pressure rise for variation of (a) Rotation parameter γ (b) Weissenberg number We.

4.5. Concentration Distribution

Figures 12 and 13 illustrate the concentration profiles $\sigma(y)$ against the y- axis for different parameters such as Brinkman number Br, Schmidt number Sc, first order chemical reaction parameter $D2$, rotation parameter γ. Figure 12(a) demonstrates a remarkable enhancement in the dimensionless concentration profile with rising magnitude of Br. Since Br increasing accelerates mass transfer through the fluid layers, resulting in raising the concentration distribution throughout the channel. A similar impact on the concentration profile is observed for increasing Schmidt number Sc which leads to reduce in molecular diffusion via Figure 12(b). A reduction in the concentration profile is noticed via Figure 13(a) with an increasing first- order chemical reaction parameter $D2$ yields a reduction in the interfacial mass transfer rate which diminishes concentration. Figure 13(b) portrays the increasing effect of the rotation parameter (γ)on $\sigma(y)$ due to induce Coriolis forces.

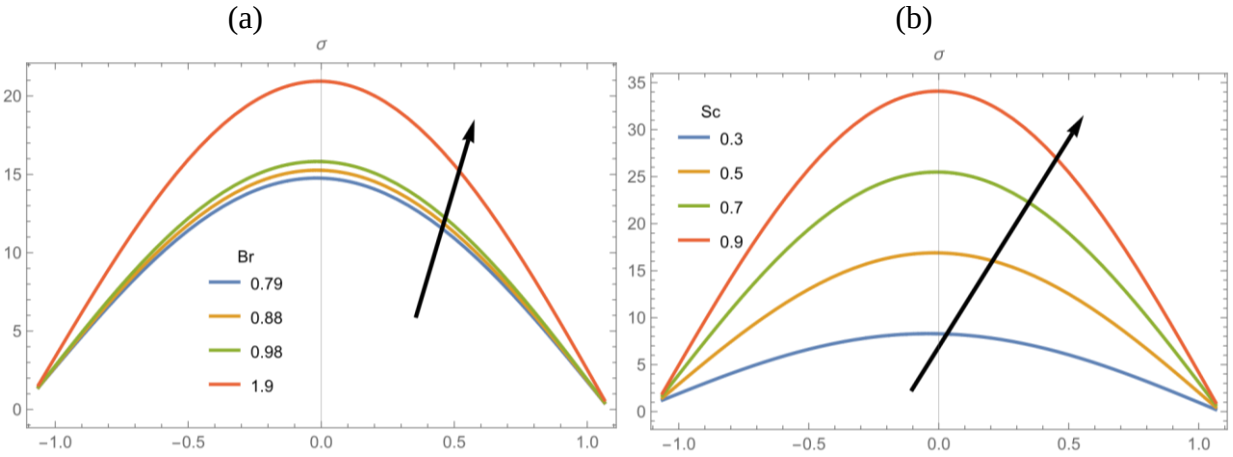


Figure 12: Concentration profile for variation of (a) Brinkman number Br (b) Schmidt number Sc.

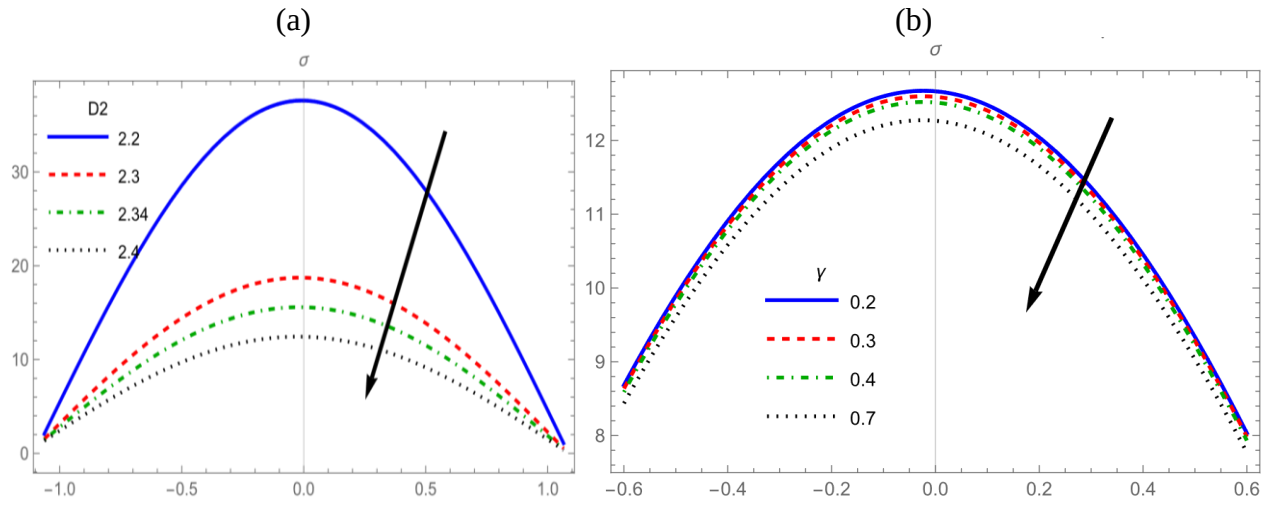


Figure 13: Concentration profile for variation of (a) first-order chemical reaction parameter *D2* (b) Rotation parameter γ.

4.6. Trapping Phenomenon

A formation of self-contained fluid mass internally circulating by closed streamlines within the flow field topology is called a trapping bolus, which forwards at a velocity identical to the driving peristaltic waves. This phenomenon witnessed a major application especially in food industry, physiology, engineering, and medicine. In this subsection the impacts of interesting Physical parameters such as rotation parameterγ, Hartmann number Ha, Darcy number Da, electro-osmotic velocity parameterU_{hs}, Weissenberg number We, flexible/compliant wall elastance parameters $E1, E2, E3$ on the trapping phenomenon are investigated through Figures 14 to 18. An increase in the rotation parameter γ causes elevation of the trapped bolus, as seen by comparing the two plots. Contour values in the center and peak regions near $(x = 1.8)$ get rise (more positive) values see Figure 14(a) and (b). However, Figures 15(a) and (b) depict that elevating Ha number leads to a reduction in the tapped bolus. The maximum core values shrink from $(-0.357\ to\ -0.450)$, this result is due to Lorentz force which resists the flow. Figures 16(a) and (b), illustrate that enhancing the Darcy number (Da) leads to an increase in the contour values across the domain. Comparing Figures 17(a) and (b), one can observed that higher values of U_{hs} enlarges the size of the trapped bolus in the central part near $(x = 0.8)$ from $(-0.33$ to $-0.324)$. Figure 18(a) and (b) demonstrate that a higher we increases the contours magnitude throughout the channel. This enhancement occurs because higher we enlarge fluid elasticity within fluid, which increasing transport across the channel width. Increasing the wall elasticity parameters $E1, E2, E3$ leads to higher contour magnitudes and volumes throughout the flow domain. Physically, higher wall compliance reduces boundary resistance and allows the flexible walls to deform more effectively, thereby enhancing wave-driven transport and elevating the distribution profiles see Figure 19.

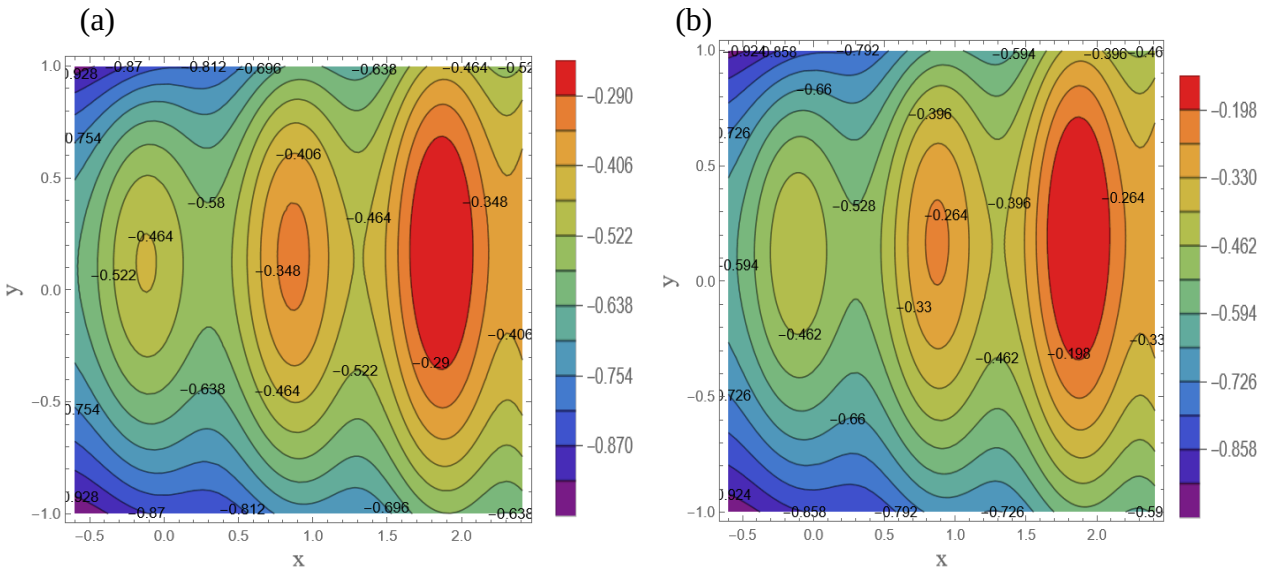


Figure 14: Streamlines for multiple magnitude of Rotation parameter $\gamma = \{0.1, 0.7\}$.

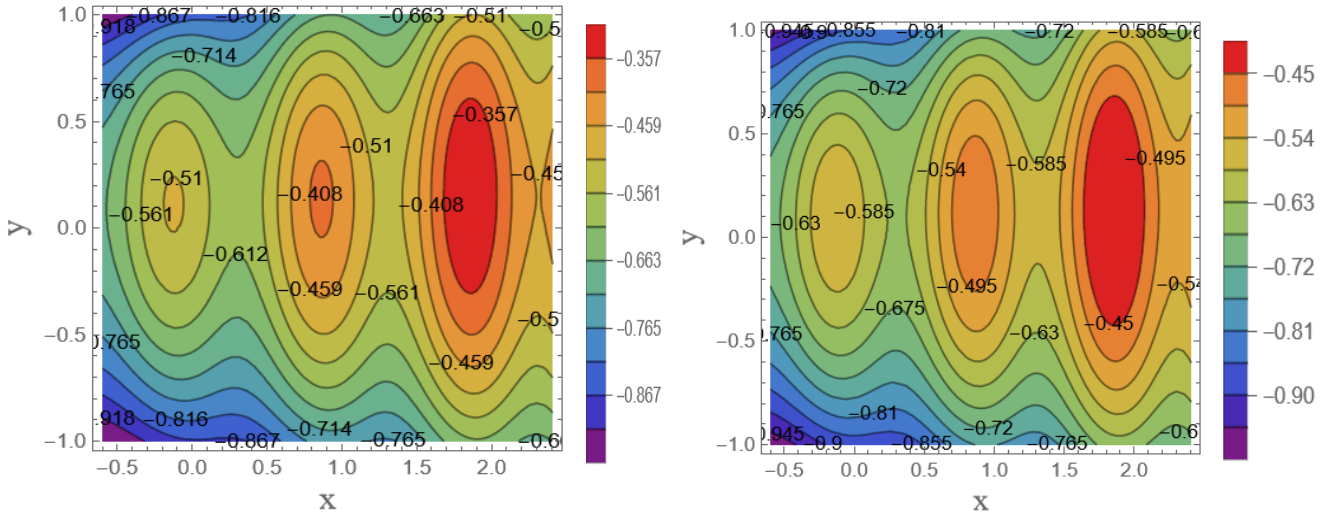


Figure 15: Streamlines for multiple magnitude of Hartmann number Ha={0.2, 0.8}

(a) (b)

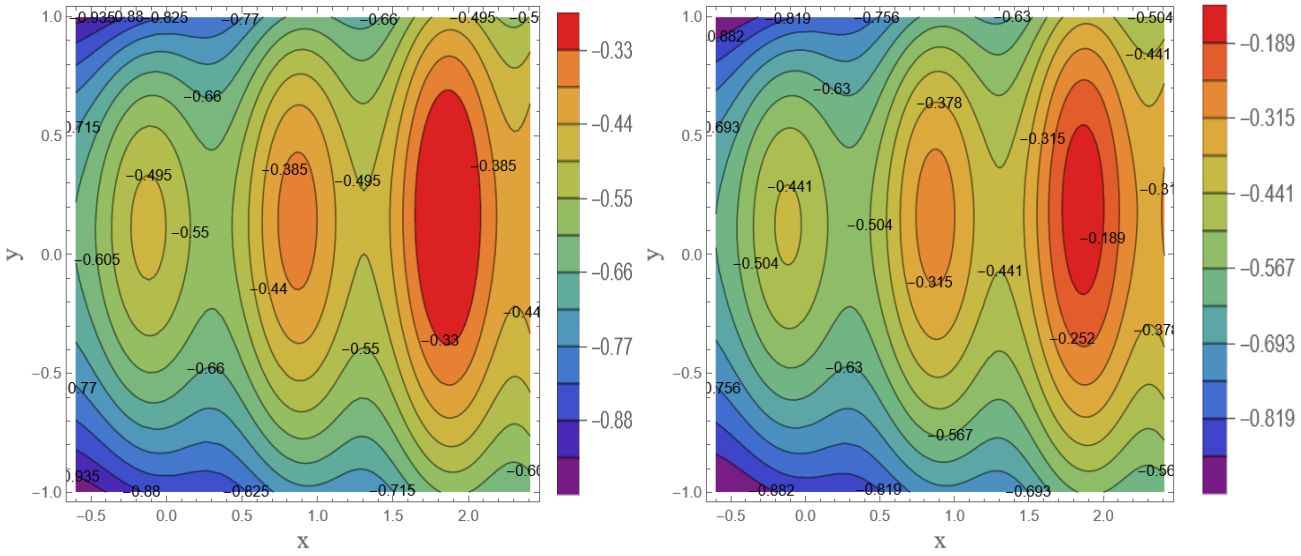


Figure 16: Streamlines for multiple magnitude of Darcy number Da ={1.2, 1.8}

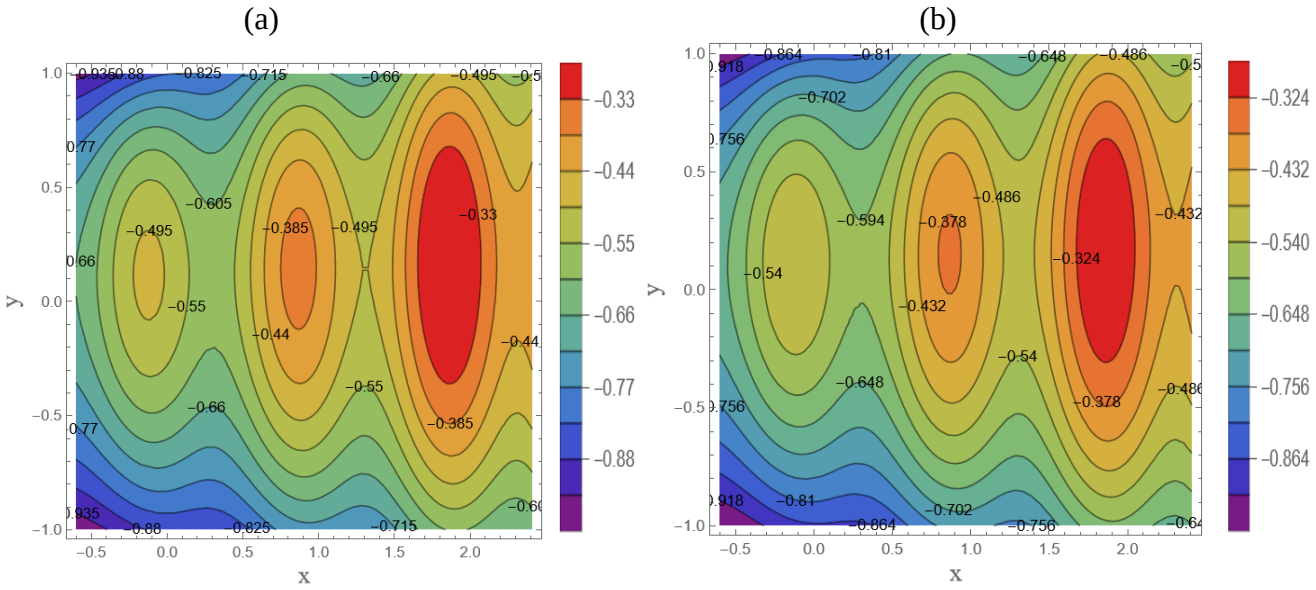


Figure 17: Streamlines for multiple magnitude of electro-osmotic velocity U_{hs} ={0.6, 0.8}

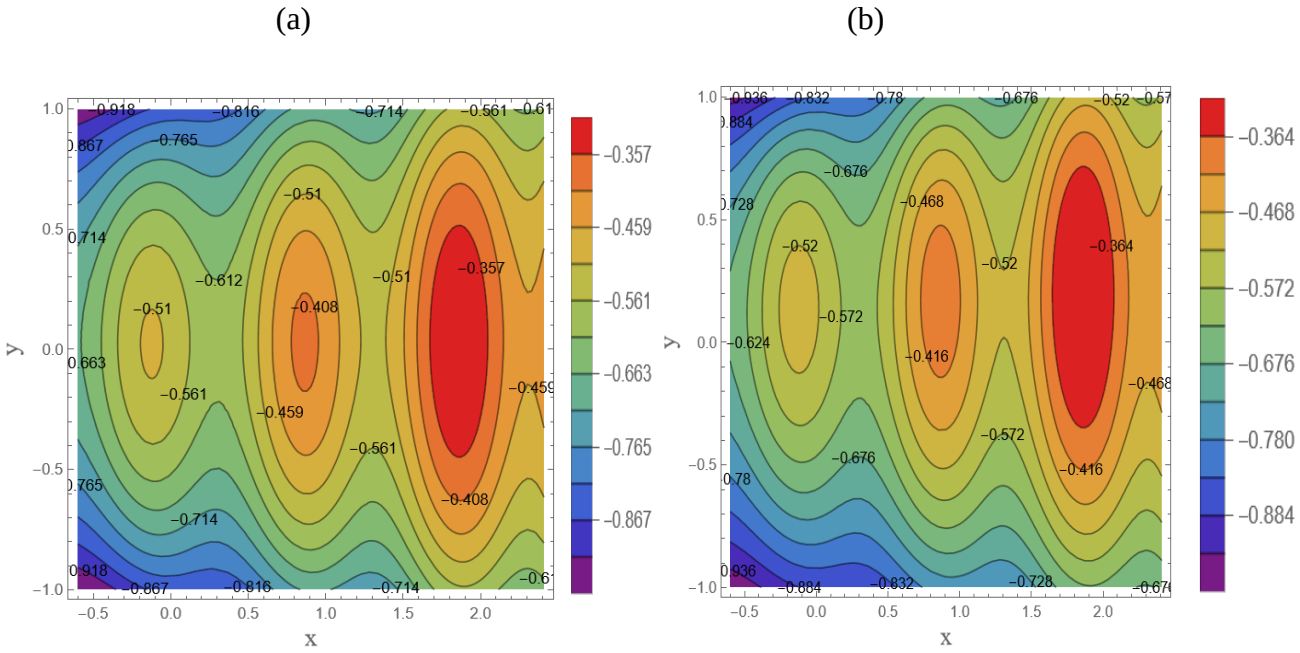


Figure 18: Streamlines for multiple magnitude of Williamson Parameter We={0.5, 0.9}

(a) (b)

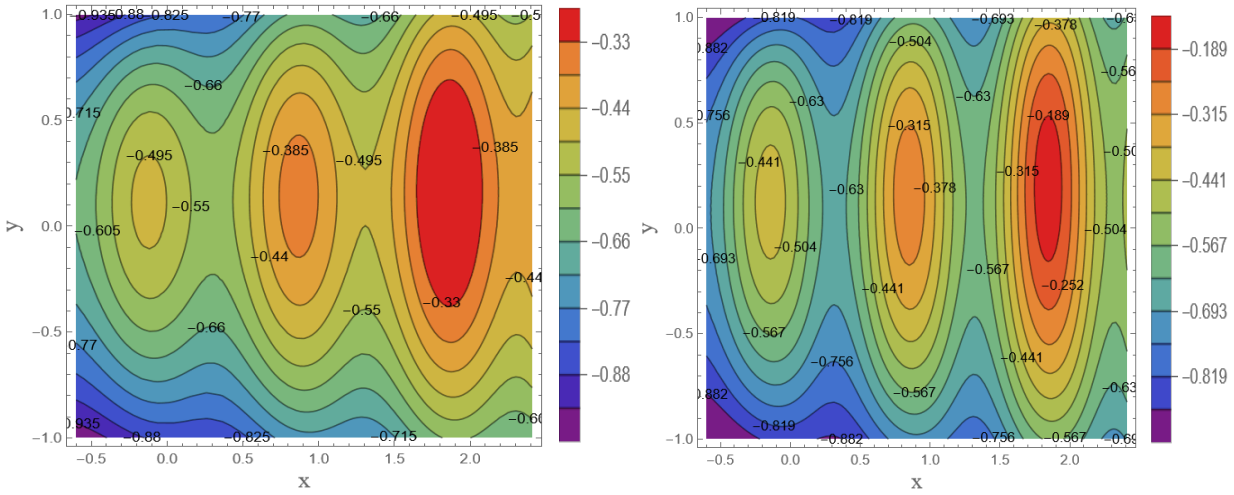


Figure 19: Streamlines for multiple magnitude of wall elasticity parameters $E1 = \{0.01,0.02,0.03\}, E2 = \{0.02,0.03,0.04\}, E3 = \{0.03,0.04,0.05\}$.

5. Conclusions

This study numerically investigated the peristaltic flow of a Willamson nanofluid through a non-uniform, inclined, tapered, asymmetric channel. The mathematical model accounted for the coupled impacts of inclined magnetic field, porous medium, thermal radiation and electro-osmotic field. Applying long-wavelength and low Reynolds number approximations, the governing non-linear differential equations were simplified and solved using ND-Solve built in Mathematica 13.

1. The velocity profile shows decreasing effect for larger Hartmann number, and Wall elasticity parameter $E1$, whereas an increment in Williamson Parameter We , Rotation parameter γ and Helmholtz–Smoluchowski velocity U_{hs} enlarge the velocity profile. This specific hydrodynamic result matched with the established findings of Hasen & Abdulhadi [5].
2. The variation of temperature distribution (θ) was found dependent on enhancing Brinkman number (Br) and Hartmann number (Ha) resulting into enhancement due to its impact on internal viscous dissipation and Ohmic Joule heating process. However, when Rd (thermal radiation parameter), Rotation parameter γ, Willamson parameter We are increased, an opposite trend was noted in terms of drop down of θ values.
3. The concentration particle profile enlarges as Brinkman number Br and Schmidt number Sc rise. Conversely, a reduction effect for first-order chemical reaction parameter $D2$ and rotation parameter γ on concentration profile is observed.
4. The increase in value of rotation parameter γ, and Williamson Parameter We reduce that axial pressure gradient $(\mathrm{dp/dx})$. However, higher U_{hs} and m_e , decrease $(\mathrm{dp/dx})$. It is seen that the peristaltic pumping region decreases with increase in Da , γ and We while enlarge Ha numbers enhance peristalsis pump region $(\Delta \mathrm{P} > 0)$.
5. The phenomena of trapping were examined where there is formation of bolus inside the tube during operation. The trapped bolus shrinks in size due to increase value of Ha, whereas increase in size and numbers of bolus is noticed for higher Da , γ and We, and $E1, E2, E3$.

References

[1] Hasen, S. S., Kareem, R. S., & Ali, H. A. (2022). Mathematical Analysis of Peristaltic Pumps for Fene-P model subject to Hall and Joule impact. *Iraqi Journal of Science*, 3141-3152.

[2] Misra, J. C., & Pandey, S. K. (2006). Peristaltic transport of physiological fluids. In *Biomathematics: modelling and simulation* (pp. 167-193).

[3] Latham TW. Fluid motions in a peristaltic pump. Massachusetts Institute of Technology; 1966.

[4] Shapiro AH, Jaffrin MY, Weinberg SL. Peristaltic pumping with long wavelengths at low Reynolds number. J Fluid Mech. 1969;37(4):799–825. https://doi.org/10.24996/ijs.2022. 63.3.29.

[5] Hasen, S. S., & Abdulhadi, A. M. (2021). Analytical Study of Soret and Dufour effect in the Electro-osmotic peristaltic flow of Rabinowitsch fluid model. *Ibn AL-Haitham Journal For Pure and Applied Sciences*, *34*(2), 70-86.

[6] Nassief, A. M., & Abdulhadi, A. M. (2024). Peristaltic Transport of Non-Newtonian Fluid under Effects of Magnetic Force and Heat Transfer in a Symmetric Channel through a Porous Medium. *Baghdad Science Journal*, *21*(4), 3.

[7] Butt, Z. I., Ahmad, I., Raja, M. A. Z., & Shoaib, M. (2026). Radiative magneto-thermal modeling of tri hybrid nanofluid in blood: A Biomedical intelligent framework for hyperthermia cancer therapy. *Journal of Thermal Biology*, 104382.

[8] Ali, H. A., Abdulhadi, A. M., Hassan, S. S., & Kashem, B. E. (2024). MHD Flow of Jeffery Nanofluid Through Symmetric Ciliated Channel with Porous Medium: Biological Application. *Iraqi Journal of Science*, 2052-2064.

[9] Nadeem, S., Akram, S., & Akbar, N. S. (2013). Simulation of heat and chemical reactions on peristaltic flow of a Williamson fluid in an inclined asymmetric channel.

[10] Akram, S., Nadeem, S., & Hanif, M. (2013). Numerical and analytical treatment on peristaltic flow of Williamson fluid in the occurrence of induced magnetic field. *Journal of Magnetism and Magnetic Materials*, *346*, 142-151.

[11] Hayat, T., Batool, N., Yasmin, H., Alsaedi, A., & Ayub, M. (2016). Peristaltic flow of Williamson fluid in a convected walls channel with Soret and Dufour effects. *International Journal of Biomathematics*, *9*(01), 1650012.

[12] Reddappa, B., Parandhama, A., & Sreenadh, S. (2020). Peristaltic transport of conducting Williamson fluid in a porous channel. *J. Math. Comput. Sci*, *10*(2), 277-288.

[13] Al-Khafajy, D., & Al-Delfi, W. N. (2023). The peristaltic flow of Williamson fluid through a flexible channel. *Iraqi Journal of Science*, 865-877.

[14] MM, M. A., Eldabe, N. T., Abouzeid, M. Y., & Ouaf, M. E. (2024). Electro-osmotic effect on the peristaltic flow of Williamson nanofluid through a porous medium in the presence of activation energy and modified Darcy's law. *Indian Journal of Chemical Technology (IJCT)*, *31*(2), 257-270.

[15] Nahi, H., & Hatem, M. (2025). Effect of the slip conditions with rotation, wall properties and heat transfer on peristaltic transport MHD. *Iraqi Journal of Science*, 1260-1273.

[16] Abdulhadi, A. M., & Al-Hadad, A. H. (2016). Effects of rotation and MHD on the Nonlinear Peristaltic Flow of a Jeffery Fluid in an Asymmetric Channel through a Porous Medium. *Iraqi journal of science*, *57*(1A), 223-240.

[17] Bandopadhyay, A., Tripathi, D., & Chakraborty, S. (2016). Electroosmosis-modulated peristaltic transport in microfluidic channels. *Physics of Fluids*, *28*(5).

[18] Mohammed, A. A., & Hummady, L. Z. (2024). The effect of heat transformation and rotation on Sutterby fluid peristaltic flow in an inclined, asymmetric channel with the porousness. *Baghdad Science Journal*, *21*(5), 9.

[19] Moeana, F. K., & Al-Khafajy, D. G. S. (2024). Analyze a temperature and MHD peristaltic flow of Sutterby fluid through a porous wave channel in a rotating frame. *Journal of Al-Qadisiyah for Computer Science and Mathematics*, *16*(1), Page-34.

[20] Hussain, S. M., Nazar, T., Shabbir, M. S., Qureshi, M. A., Jamshed, W., Makhdoum, B. M., ... & Bayram, M. (2025). Thermal radiation effects on Bingham–Papanastasiou tetra-hybrid nanofluid dynamics in a porous diseased artery with electro-osmotic flow and permeability. *Journal of Radiation Research and Applied Sciences*, *18*(2), 101575.

[21] Li, S., Imtiaz, M., Ijaz Khan, M., Kumar, R. N., & Akramova, K. S. (2026). Applications of Soret and Dufour effects for Maxwell nanomaterial by convectively heated surface. *Numerical Heat Transfer, Part A: Applications*, *87*(1), 2314224.

[22] Ramya, N., & Deivanayaki, M. (2025). Impact of Soret and dufour effects on Casson nanofluid flow in a magnetic field along with heat and mass transfer. *Indian J. Sci. Technol*, *18*(13), 1059-1070.